Adaptive, Optimal, Virtual Synchronous Generator Control of Three-Phase Grid-Connected Inverters under Different Grid Conditions—An Adaptive Dynamic Programming Approach

Zhongyang Wang, Yunjun Yu*, *Member, IEEE*, Weinan Gao*, *Member, IEEE*, Masoud Davari*, *Senior Member, IEEE*, and Chao Deng, *Member, IEEE*

Abstract—This paper proposes an adaptive, optimal, data-driven control approach based on reinforcement learning and adaptive dynamic programming (commonly known as ADP) to the three-phase grid-connected inverter employed in virtual synchronous generators (VSGs). This article takes into account unknown system dynamics and different grid conditions, including balanced/unbalanced grids, voltage drop/sag, and weak grids. The proposed method is based on value iteration, which does not rely on an initial admissible control policy for learning. Considering the premise that the VSG control should stabilize the closed-loop dynamics, the VSG outputs are optimally regulated through the adaptive, optimal control strategy proposed in this work. Comparative simulations and experimental results validate the proposed method's effectiveness and reveal its practicality and implementation.

Index Terms—Adaptive dynamic programming (ADP); adaptive, optimal control; reinforcement learning; value iteration; virtual synchronous generator (VSG).

This work was supported in part by Fujian Province Young and Middle-aged Teacher Education Research Project (JAT200901), National Natural Science Foundation of China (NSFC: 61563034), and International S&T Cooperation Program of China (ISTCP: 2014DFG72240). The work of Weinan Gao was supported by the U.S. National Science Foundation (U.S. NSF) under CMMI Award #2138206 granted by the Engineering Research Initiation program. The work of Masoud Davari was supported by the U.S. NSF under ECCS-EPCN Awards #1808279 and #1902787 granted by the core program of Energy, Power, Control, and Networks (EPCN) in the Division of Electrical, Communications and Cyber Systems (ECCS). This work was also supported in part by dSPACE GmbH Company, SEMIKRON Company, and Verivolt Company for the Laboratory for Advanced Power and Energy Systems (LAPES)-which Masoud Davari has founded, established, and directed at Georgia Southern University-where the experiments of this research were entirely conducted. (*Corresponding authors: Yunjun Yu; Weinan Gao; Masoud Davari.)

Zhongyang Wang is with the School of Applied Science and Engineering, Fuzhou Institute of Technology, Fuzhou, 350506, China (e-mail: wzy11329@gmiot.com; zywangncu@163.com).

Yunjun Yu is with the Department of Automation, Information Engineering School, Nanchang University, Nanchang, 330031, China (e-mail: yuyunjun@ncu.edu.cn).

Weinan Gao is with the Department of Mechanical and Civil Engineering, College of Engineering and Science, Florida Institute of Technology (Florida Tech), Melbourne, FL 32901 USA (e-mail: wgao@fit.edu).

Masoud Davari is with the Department of Electrical and Computer Engineering, Georgia Southern University (Statesboro Campus), Statesboro, GA 30460 USA (e-mail: mdavari@georgiasouthern.edu; davari@ualberta.ca).

Chao Deng is with the Institute of Advanced Technology, Nanjing University of Posts and Telecommunications, Nanjing 210023, China (e-mail: dengchao@njupt.edu.cn; dengchao_neu@126.com).

I. Introduction

ONSIDERING climate change and global warming, photovoltaic (solar cell) systems are integrated into modernized power systems more and more. Photovoltaic systems [as one of the promising inverter-based resources (IBRs)] become practical alternatives to fossil-fuel-based distributed energy resources (DERs) to generate electricity [1]. On the one hand, IBRs are not usually involved in the frequency control in power networks because of having no inertia—contrary to traditional fossil-fuel-based DERs. On the other hand, several researchers have recently proposed a droop-based control scheme to improve power sharing and stability of various DERs in microgrids [2]–[4].

In microgrid applications, the droop control obtains stable frequency and voltage through P/f and Q/V, respectively. It has been shown that both optimization of the droop coefficient and the additional droop control loop can improve system stability [5], [6]. However, IBRs with droop control still do not have inertial support for the power system. In order to simulate the damping and inertia of synchronous generators, a new method is proposed—called virtual synchronous generator (VSG) [7]–[9]. The VSG has damping characteristics and virtual inertia, which can emulate the synchronous generators' characteristics [10]–[12]. The VSG scheme and droop control have been applied to IBRs [14], [15]. Both methods can effectively bring renewable energy penetration into the grid and ensure that the grid-connected system operates independently.

In [16], an adaptive control strategy for VSGs has been proposed. This strategy constructs the virtual inertia and the relationship between the damping and the frequency offset. As a result, the system can freely configure the virtual inertia and damping coefficient according to the system characteristics at different stages of the transient process. However, the control strategy does not have any performance index to judge whether it is optimal or not.

In [17], a small signal model has been established. Also, the proposed VSG model's parameters have been optimized in order to deal with various criteria as constraints—e.g., the steady-state response, transient response, and stability. However, these criteria are significantly affected by each other, and it is difficult to balance multiple performance indicators.

Aiming at damping power oscillations, the authors of [18] have proposed an adaptive virtual inertia control strategy, elaborating the concept of variable virtual inertia and negative virtual inertia. Still, the value of virtual inertia in this scheme adopts Bang-Bang control. As a result, the introduced virtual inertia frequent changes of power will cause power jitter.

The fault-ride-through (FRT) capability [also known as lowvoltage-ride-through capability in literature and connection to weak grids are among the two critical considerations in VSG-related studies. Once there is a voltage drop/sag caused by faults, the VSG will encounter transient stability problems similar to traditional synchronous generators [19]-[21]. Relevant scholars have done a lot of research on VSG voltage drop conditions [22]–[24]. Also, due to the large transmission line impedance, grid-connected renewables can be integrated into and working under weak-grid conditions—thereby affecting the system stability—see [25], [26] and references therein. In order to improve the inductance of the circuit, a virtual impedance is usually added to the control loop [27]. However, no matter whether it is an FRT capability or integration into weak-grid condition, the power loop has not been improved. The system will produce some unnecessary oscillations or overshoot.

In recent years, VSG optimization has been employed to improve the transient characteristics of output frequency and power by adjusting virtual inertia and damping coefficient. However, tunning the VSG parameters is still a practical conundrum when the system dynamics are unknown. If the control parameters are poorly tuned, the VSG output response speed and oscillation cannot be satisfied simultaneously, which significantly affects the overall system performance.

VSG can be approximated as a linear system [28]; the standard solution to control a linear system in an optimal sense is a linear quadratic regulator (LQR), but the LQR method requires the perfect knowledge of all the system parameters. In order to solve such problems, the reinforcement learning theory (see [29]) and adaptive dynamic programming (ADP) for non-model-based, data-driven, adaptive, optimal control design are deemed appropriate and fit. In general, a reinforcement learning problem requires the existence of an agent to be able to interact with an unknown environment by taking appropriate actions and receiving rewards from it. In [29], the authors have defined the reinforcement learning ratio as to how to map a context to an action to maximize the digital reward signal. The goal of reinforcement learning is to learn an optimal policy to solve the effective index of the optimal algorithm of maximization or minimization under certain constraints. Reinforcement learning currently has some actual applications, such as power systems, connected vehicles, and industrial processes [30]–[32].

This paper proposes a new control scheme for VSG based on the ADP algorithm. ADP is an adaptive, optimal control algorithm for dynamic systems [33], [34]. One of the problems that ADP aims to address for linear control systems is known as the linear optimal output regulation problem (LOORP) [35], [36]; it is required to solve the algebraic Riccati equation to obtain the optimal controller [37], [38]. Reinforcement learning and ADP are considered for improving the transient

response of power systems; for example, see [39].

In order to overcome the problem, ADP advances on the theory of optimal control by solving optimal control problems with unknown dynamics [36], [40], [41]. Currently, both value iteration and policy iteration can be used to implement ADP [42]–[44]. The main difference between the two approaches is that value iteration does not require an initial stabilizing control policy [42], while the policy iteration involves the knowledge of an initial stabilizing control policy. Due to the system uncertainty in the considered problem formulation, an initial stabilizing controller cannot be obtained. Therefore, this research uses the value iteration strategy. Also, this article increases the convergence speed using ADP to speed up the system's time response [45].

In this study, the VSG dynamics are described via a linear dynamic system. In case of bad parameter tuning, adjusting the real-time input data is necessary, according to the observed angular frequency and active power error. Thus, transients of the system output frequency are being optimized.

The rest of this paper is organized as follows. Section III introduces the VSG control algorithm for grid-connected inverters and establishes a linear error model. Section III provides the calculations of the VSG reference currents under different practical cases and various scenarios. Section IV analyzes the VSG low voltage ride-through. Section V discusses the VSG weak-grid conditions. Section VI details the LQR problem and—via the ADP method—designs the value iteration method to find the optimal control law recursively when the system model is not entirely and accurately known. Section VII presents simulations of analyses. Section VIII presents experiments to show the effectiveness of the proposed method. Section IX concludes the contributions of this article.

Notations: Throughout this article, \otimes indicates the Kronecker product operator. For a symmetric matrix $P \in \mathbb{R}^{m \times m}$, an asymmetric matrix $Y \in \mathbb{R}^{n \times m}$, and a column vector $v \in \mathbb{R}^n$, operator "vecs," "vec," and "vecv" denote $\text{vecs}(P) = [p_{11}, 2p_{12}, \cdots, 2p_{m-1,m}, p_{mm}]^T \in \mathbb{R}^{\frac{1}{2}m(m+1)}$, $\text{vec}(Y) = [y_1^T, y_2^T, \cdots, y_m^T]^T \in \mathbb{R}^{mn}$ with $y_i \in R^n$, and $\text{vecv}(v) = [v_1^2, v_1v_2, \cdots, v_1v_n, v_2^2, v_2v_3, \cdots, v_{n-1}v_n, v_n^2]^T \in \mathbb{R}^{\frac{1}{2}n(n+1)}$, respectively.

II. SYSTEM MODELING

A. Modeling of VSG

A block diagram of a grid-connected inverter based on VSG control is shown in Fig. 1. As shown in Fig. 1, the grid side and inverter side are connected through an LC-filter, which is commonly used in voltage-sourced converters. The grid voltage phase is tracked by a phase-locked loop (also known as PLL).

The output voltage U_o^* is obtained through the VSG algorithm. The voltage and current controller is a proportional-integral controller that compares the reference voltage and the output voltage to generate the reference voltage V^* . Finally, the switching signal is generated through pulse-width modulation (PWM). The VSG control algorithm includes active-

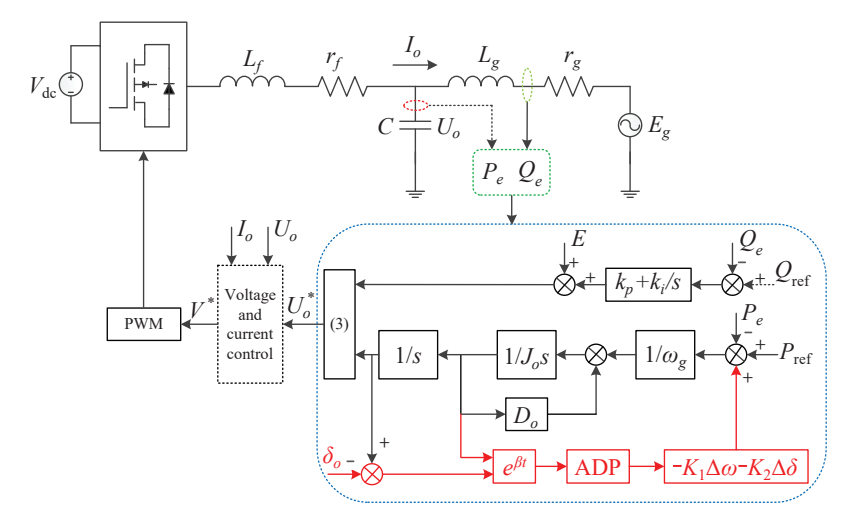


Fig. 1. Block diagram of a grid-connected inverter based on VSG control.

frequency and reactive-voltage control methods. VSG control is expressed as

$$\begin{cases} \dot{\delta}(t) = \omega(t) - \omega_g \\ J_o \omega_g \dot{\omega}(t) = P_{\text{ref}} - P_e - D_o \omega_g(\omega(t) - \omega_g) \end{cases}$$

and

$$U = E + \left(K_p + \frac{K_i}{s}\right)(Q_{\text{ref}} - Q_e) \tag{2}$$

where $P_{\rm ref}$ and $Q_{\rm ref}$ are the references of active and reactive power, respectively; P_e and Q_e are the outputs of active and reactive power, respectively; $\delta(t)$ is the output power angle; $\omega(t)$ is the output angular frequency; ω_g is the grid angular frequency; D_o is the damping coefficient; J_o is the inertia constant; E is the grid voltage amplitude; and U is the VSG output voltage amplitude.

The output voltage of VSG is

$$U_o^* = \begin{bmatrix} U \sin(\omega_g t + \delta(t)) \\ U \sin(\omega_g t - \frac{2\pi}{3} + \delta(t)) \\ U \sin(\omega_g t + \frac{2\pi}{3} + \delta(t)) \end{bmatrix}$$

$$U_{od}^* = U \cos \delta \quad \text{and} \quad U_{og}^* = U \sin \delta. \tag{3}$$

B. VSG Parameter Tuning

By [47], the output power of the inverter can be expressed as

$$S = P_e + jQ_e$$

$$= \frac{r_g E_g U_o \cos \delta(t) - r_g E_g^2 + X E_g U_o \sin \delta(t)}{r_g^2 + X^2} + j \frac{X E_g U_o \cos \delta(t) - X E_g^2 - r_g E_g U_o \sin \delta(t)}{r_o^2 + X^2}$$
(4)

where $X = \omega_q L_q$.

Now, considering line impedance and impedance angle as

$$\begin{cases}
Z = \sqrt{(\omega_g L_g)^2 + r_g^2} \\
\alpha = \arctan \frac{\omega_g L_g}{r_g}
\end{cases}$$
(5)

the output power of VSG is

$$(1) \begin{cases} P_e = \frac{(U_o E_g \cos \delta(t) - E_g^2) \cos \alpha + U_o E_g \sin \alpha \sin \delta(t)}{Z} \\ Q_e = \frac{(U_o E_g \cos \delta(t) - E_g^2) \sin \alpha - U_o E_g \cos \alpha \sin \delta(t)}{Z} \end{cases}$$
 (6)

Since the line impedance is mainly inductive, i.e., $X>>r_g$, $\alpha\approx 90^\circ$. Therefore, the simplified expressions for active and reactive power are

$$P_e = \frac{U_o E_g}{X} \sin \delta(t)$$

$$Q_e = \frac{U_o (U_o - E_g)}{X}$$
(7)

Since the VSG output power angle is small, it can be assumed $\sin\delta\approx\delta$. Then,

$$\begin{cases} P_e = \frac{U_o E_g}{X} \sin \delta(t) = \frac{U_o E_g}{X} \delta(t) \\ \dot{P}_e = \frac{U_o E_g}{X} \dot{\delta}(t) = \frac{U_o E_g}{X} (\omega(t) - \omega_g) . \end{cases}$$

$$(8)$$

$$\ddot{P}_e = \frac{U_o E_g}{X} \dot{\omega}(t)$$

Equation (1) can be expressed as

$$P_{\text{ref}} = P_e + \frac{DX}{U_o E_a} \dot{P}_e + \frac{JX}{U_o E_a} \ddot{P}_e \tag{9}$$

with $D = D_o \omega_g$ and $J = J_o \omega_g$. After Laplace transform, one gets

$$\frac{P_e(s)}{P_{\text{ref}}(s)} = \frac{\omega_n^2}{s^2 + 2\omega_n \xi s + \omega_n^2}$$
 (10)

where
$$\omega_n = \sqrt{\frac{U_o E_g}{JX}}$$
 and $\xi = \frac{D}{2} \sqrt{\frac{X}{JU_o E_q}}$.

As a result, the VSG parameters are able to adjust, impact, and tune the time response characteristics according to (10). In general, in the process of virtual damping tuning, the inertia J and the damping factor D are tuned through the optimal damping ratio method for linear second-order systems [46]. The system's damping ratio is defined at $\xi = 0.707$, i.e.,

$$D = \sqrt{2J \frac{U_o E_g}{X}}. (11)$$

C. State Space Representation on VSG

Because of the original system uncertainty, it is necessary to increase the control input u(t) in the original system in order to eliminate the uncertainty

$$\Delta \dot{\omega}(t) = -\frac{D}{J} \Delta \omega(t) - \frac{1}{J} P_e(t) + \frac{1}{J} P_{\text{ref}} + \frac{1}{J} u(t)$$

$$= -\frac{D}{J} \Delta \omega(t) - \frac{1}{J} \Delta P(t) + \frac{1}{J} u(t)$$

$$= -\frac{D}{J} \Delta \omega(t) - \frac{U_o E_g}{J X} \Delta \delta(t) + \frac{1}{J} u(t)$$
(12)

with $\Delta\delta(t) = \delta(t) - \delta_o$, $\Delta\omega(t) = \omega(t) - \omega_g$. $x(t) = \begin{bmatrix} \Delta\delta(t) & \Delta\omega(t) \end{bmatrix}^T$ is assumed; the new equation of VSG can be written as

$$\dot{x}(t) = Ax(t) + Bu(t) \tag{13}$$

with
$$A = \begin{bmatrix} 0 & 1 \\ -\frac{U_o E_g}{JX} & -\frac{D}{J} \end{bmatrix}$$
 and $B = \begin{bmatrix} 0 \\ \frac{1}{J} \end{bmatrix}$. The control goal is to find the optimal feedback control gain

in u(t) = -Kx(t). The optimal feedback gain matrix K can be obtained according to the knowledge of ADP when system parameters are unknown.

III. REFERENCE CURRENT CALCULATION

Under unbalanced grid voltages, the instantaneous complex power output by the grid-connected inverter is expressed as

$$S = U_{o\alpha\beta}\hat{I}_{o\alpha\beta} = \frac{3}{2}(U_{odq}^{+} + U_{odq}^{-})(\hat{I}_{odq}^{+} + \hat{I}_{odq}^{-})$$

$$= P_{e} + jQ_{e}$$
(14)

where the superscript "\" represents the conjugate, "+" represents positive order, and "-" represents negative order.

The instantaneous active power is found as follows, respectively (see [48]).

$$P_e = \text{Re}(S) = P_0 + P_c \cos(2\omega_q t) + P_s \sin(2\omega_q t)$$
 (15)

where

$$\begin{cases}
P_0 = 1.5(U_{od}^+ I_{od}^+ + U_{oq}^+ I_{oq}^+ + U_{od}^- I_{od}^- + U_{oq}^- I_{oq}^-) \\
P_c = 1.5(U_{od}^- I_{od}^+ + U_{oq}^- I_{oq}^+ + U_{od}^+ I_{od}^- + U_{oq}^+ I_{oq}^-) \\
P_s = 1.5(U_{oq}^- I_{od}^+ - U_{od}^- I_{oq}^+ - U_{oq}^+ I_{od}^- + U_{od}^+ I_{oq}^-)
\end{cases} (16)$$

1) Output Current References: To ensure that the output current is balanced, the negative sequence component of the current is required to be 0

$$I_{od}^{*-} = 0 \quad I_{oq}^{*-} = 0.$$
 (17)

2) Constant Active Power Control: In order to eliminate active power oscillations, P_c and P_s in (16) should be set to 0, which can be expressed as

$$\begin{bmatrix} U_{od}^{-} & U_{oq}^{-} \\ U_{oq}^{-} & -U_{od}^{-} \end{bmatrix} \begin{bmatrix} I_{od}^{*+} \\ I_{oq}^{*+} \end{bmatrix} + \begin{bmatrix} U_{od}^{+} & U_{oq}^{+} \\ -U_{oq}^{+} & U_{od}^{+} \end{bmatrix} \begin{bmatrix} I_{od}^{*-} \\ I_{oq}^{*-} \end{bmatrix} = \begin{bmatrix} 0 \\ 0 \end{bmatrix}$$
(18)

In addition, (18) can be written a

$$\begin{bmatrix} I_{od}^{*-} \\ I_{oq}^{*-} \end{bmatrix} = -\frac{1}{K} \begin{bmatrix} K_1 & K_2 \\ K_2 & -K_1 \end{bmatrix} \begin{bmatrix} I_{od}^{*+} \\ I_{oq}^{*+} \end{bmatrix}$$
(19)

where
$$K = (U_{od}^+)^2 + (U_{oq}^+)^2$$
, $K_1 = U_{od}^+ U_{od}^- - U_{oq}^+ U_{oq}^-$, and $K_2 = U_{od}^+ U_{oq}^- + U_{oq}^+ U_{od}^-$.

The positive sequence current is given by

$$\begin{cases}
I_{od}^{*+} = (K_{1p} + \frac{K_{1i}}{s})(U_{od}^* - U_{od}^+) - \omega C U_{oq}^+ \\
I_{oq}^{*+} = (K_{1p} + \frac{K_{1i}}{s})(U_{oq}^* - U_{oq}^+) + \omega C U_{od}^+
\end{cases}$$
(20)

Here, the current control loop adopts a proportional-integral controller as

$$\begin{cases} V_d^{*+} = (K_{2p} + \frac{K_{2i}}{s})(I_{od}^{*+} - I_{od}^+) - \omega L_f I_{oq}^+ \\ V_q^{*+} = (K_{2p} + \frac{K_{2i}}{s})(I_{oq}^{*+} - I_{oq}^+) + \omega L_f I_{od}^+ \\ V_d^{*-} = (K_{2p} + \frac{K_{2i}}{s})(I_{od}^{*-} - I_{od}^-) + \omega L_f I_{oq}^- \\ V_q^{*-} = (K_{2p} + \frac{K_{2i}}{s})(I_{oq}^{*-} - I_{oq}^-) - \omega L_f I_{od}^- \end{cases}$$

$$(21)$$

IV. GRID VOLTAGE DROP FOR FRT CAPABILITY

A. Fault Current and Power Angle Characteristics

During a voltage drop, define the grid voltage as $E'_a \angle 0$, the VSG output voltage is $U'_{o} \angle \delta'(t)$, and the VSG output frequency is $\omega'(t)$. The power angle of VSG during fault can be expressed as

$$\delta'(t) = \int (\omega'(t) - \omega_g)dt. \tag{22}$$

The current output of VSG during fault is

$$\vec{I_o}'(t) = \frac{U_o' \angle \delta'(t) - E_g'}{r_o + i\omega_o L}$$
 (23)

where

$$|I'_o(t)| = \frac{1}{|Z|} \sqrt{E'^2_g + U'^2_o - 2E'_g U'_o \cos \delta'(t)}.$$
 (24)

From (24), it is obvious that when the grid voltage drops to a certain extent, the VSG output current is mainly related to the power angle of the VSG output voltage during fault.

$$\begin{split} \frac{\partial |I'_o(t)|}{\partial U'_o} &= \frac{U'_o - E'_g \cos \delta'(t)}{|Z| \sqrt{E'_g{}^2 + U'_o{}^2 - 2E'_g U'_o \cos \delta'(t)}} \\ &> \frac{U'_o - E'_g}{|Z| \sqrt{E'_g{}^2 + U'_o{}^2 - 2E'_g U'_o \cos \delta'(t)}} \\ &= \frac{X Q'_e \cos \delta'(t)}{|Z| U'_o \sqrt{E'_g{}^2 + U'_o{}^2 - 2E'_g U'_o \cos \delta'(t)}} > 0. \end{split}$$

$$\frac{\partial |I_o'(t)|}{\partial \delta'(t)} = \frac{\sqrt{2} E_g' U_o' \sin \delta'(t)}{|Z| \sqrt{E_g'^2 + U_o'^2 - 2 E_g' U_o' \cos \delta'(t)}} > 0. \quad (26)$$

From (25) and (26), it is evident that the derivative of the output current with respect to the VSG output voltage and the power angle of VSG during fault are both greater than zero. It means that after the grid voltage is reduced to a certain extent, the greater the VSG output voltage or the greater the power angle of VSG during fault, the greater the output current.

B. Power Ring Design

Before a voltage drop (or sag) caused by faults, the system has been running in the rated state, so the output power has been

$$P_e = \frac{U_o E_g}{X} \sin \delta_o. \tag{27}$$

After a voltage drop, the output power will be

$$P'_{e} = \frac{U'_{o}E'_{g}}{X}\sin\delta'_{o} = \frac{U'_{o}E'_{g}}{X}\sin(\delta_{o} + \Delta\delta'_{o})$$

$$= \frac{U'_{o}E'_{g}}{X}(\sin\delta_{o}\cos\Delta\delta' + \cos\delta_{o}\sin\Delta\delta'_{o}).$$
(28)

Assuming that after adding the power angle compensation, the power angle does not change much, i.e., $\Delta \delta'(t) \approx 0$. Therefore, $\cos \Delta \delta'(t) \approx 1$ and $\sin \Delta \delta'(t) \approx \Delta \delta'(t)$, so $\delta_o = \delta'_o$. Thus,

$$\frac{P_e'}{P_e} = \frac{P_{\text{ref}}'}{P_{\text{ref}}} = \frac{U_o' E_g'}{U_o E_g} + \frac{U_o' E_g'}{U_o E_g} \frac{\cos \delta_o}{\sin \delta_o} \Delta \delta'(t). \tag{29}$$

The new active power reference is

$$P_{\text{ref}}' = P_1 + P_2 \delta' \tag{30}$$

where

$$\begin{cases}
P_1 = \frac{U_o' E_g'}{U_o E_g} \left(1 - \delta_o \cos \delta_o \right) P_{\text{ref}} \\
P_2 = \frac{U_o' E_g'}{U_o E_g} \cos \delta_o P_{\text{ref}}.
\end{cases}$$
(31)

In the steady-state operation, if the VSG power angle and output voltage and current satisfy (23) and (24), then the power angle and output voltage and current expressions can be obtained through

$$\cos \delta_o = \frac{U_o^2 + E_g^2 - (|Z||I_o|)^2}{2U_o E_g}.$$
 (32)

Assuming that the grid voltage drops, after the active power reference is adjusted, the power angle during the fault period and the output voltage and current meet

$$\cos \delta_o' = \frac{U_o'^2 + E_g'^2 - (|Z||I_o'|)^2}{2U_o'E_g'} = \cos \delta_o.$$
 (33)

The output current tolerance range of the VSG is specified as $k_{I_{\rm Fault}}I_{o}$, in which $1.1 < k_{I_{\rm Fault}} < 1.5$, for example (depending on the current limit of the power electronic switches utilized). As a consequence—from (32) and (33)—the new VSG output voltage reference is

$$U_o' = \frac{ak + \sqrt{a^2k^2 - 4(E_g^2k^2 - k_{I_{\text{Fault}}}^2|Z|^2I_o^2)}}{2}$$
(34)

where $a=(U_o^2+E_g^2-k_{I_{\rm Fault}}^2|Z|^2I_o^2)/U_o$ and $k=E_g'/E_g$. When it is stable during a fault, the output active power and reactive power can be expressed as

$$\begin{cases} P'_{e} = \frac{3}{2} U'_{o} I'_{o} \cos \phi = P'_{\text{ref}} \\ Q'_{e} = \frac{3}{2} U'_{o} I'_{o} \sin \phi = Q'_{\text{ref}} \end{cases}$$
(35)

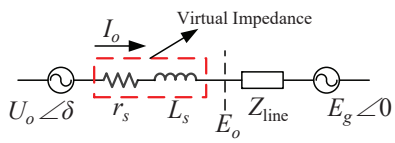


Fig. 2. VSG's stator circuit block diagram after adding virtual impedance.

where ϕ is the power factor angle. The new active power reference is

$$Q'_{\text{ref}} = \sqrt{\frac{9}{4} U_o^{\prime 2} I_o^{\prime 2} - P_{\text{ref}}^{\prime 2}}.$$
 (36)

C. State Equation During Voltage Drop

As before the voltage drop, the state space expression after the voltage drop is as follows.

$$\Delta \dot{\omega}'(t) = -\frac{D}{J} \Delta \omega'(t) - \frac{1}{J} P_e'(t) + \frac{1}{J} P_{\text{ref}}' + \frac{1}{J} u'(t)$$

$$= -\frac{D}{J} \Delta \omega(t) - \frac{K_d}{J} (\delta'(t) - \delta_o') + \frac{1}{J} u(t)$$
(37)

where
$$K_d = \frac{U'_o E'_g}{X} - P_2$$
 and $\delta'_o = \delta_o$.

V. WEAK-GRID CONDITIONS

In the previous analysis, the resistance part of the line impedance has been ignored, thinking that the line impedance is inductive. Then, when the line impedance is resistive and inductive, the VSG output active power and reactive power are

$$\begin{cases}
P_e = \frac{E_g}{Z^2} \left[(U_o - E_g) r_g + U_o X \delta(t) \right] \\
Q_e = \frac{E_g}{Z^2} \left[(U_o - E_g) X - U_o r_g \delta(t) \right]
\end{cases}$$
(38)

Next, the partial derivatives of δ and U_o for (38) are

$$\begin{cases}
\frac{\partial P_e}{\partial \delta} = \frac{U_o E_g X}{Z^2}, & \frac{\partial P_e}{\partial U_o} = \frac{E_g}{Z^2} (r_g + X \delta(t)) \\
\frac{\partial Q_e}{\partial \delta} = \frac{U_o E_g r_g}{Z^2}, & \frac{\partial Q_e}{\partial U_o} = \frac{E_g}{Z^2} (X - r_g \delta(t))
\end{cases}$$
(39)

Equation (39) shows that there exists a coupling between the active power and reactive power of the VSG under weak-grid conditions. In order to improve stability, a virtual impedance is added to the control algorithm to increase the linear inductance. Fig. 2 shows the VSG's stator circuit block diagram after adding virtual impedance. Also, Fig. 3 depicts the VSG's stator electrical equation and double closed-loop control block diagram. One can write the state space expression under weak-grid conditions as

$$\Delta \dot{\omega}''(t) = -\frac{D}{J} \Delta \omega''(t) - \frac{1}{J} P_e''(t) + \frac{1}{J} P_{\text{ref}} + \frac{1}{J} u''(t)$$

$$= -\frac{D}{J} \Delta \omega''(t) - \frac{K_d'}{J} (\delta''(t) - \delta_o'') + \frac{1}{J} u''(t)$$
(40)

where $K'_d = \frac{U_o E_g X}{Z^2}$.

VI. ADAPTIVE, OPTIMAL VSG CONTROL

In this section, an adaptive, optimal VSG control algorithm based on ADP is developed.

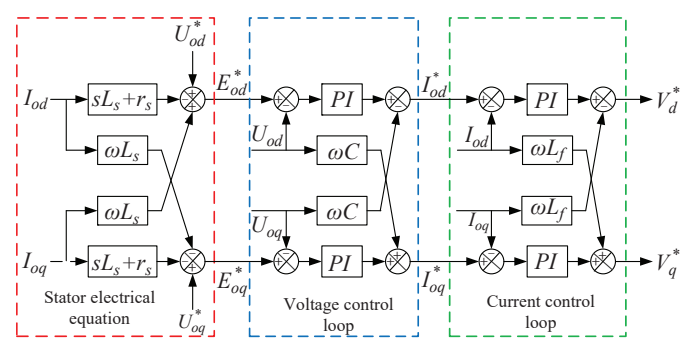


Fig. 3. VSG's stator electrical equation and double closed-loop control block diagram.

A. Problem Description

Consider the VSG system as follows.

$$\begin{cases} \dot{x}(t) = Ax(t) + Bu(t) \\ u(t) = -Kx(t) \end{cases}$$
(41)

where $x\in\mathbb{R}^n$, $u\in\mathbb{R}^m$, $A\in\mathbb{R}^{n\times n},\,B\in\mathbb{R}^{n\times m},\,K\in\mathbb{R}^{m\times n}$

The control objective finds the optimal feedback controller u=-Kx to solve the following constraint minimization expressed in Problem 1.

Problem 1.

$$\min_{u} \int_{t}^{\infty} e^{2\beta\tau} (x(\tau)^{T} Q x(\tau) + u(\tau)^{T} R u(\tau)) d\tau$$

$$subject \quad to \quad (41)$$

where $\beta \geq 0$, $Q = Q^T \geq 0$, $R = R^T \geq 0$, and (\bar{A}, \sqrt{Q}) is observable.

Then, the closed-loop system can be obtained directly

$$\dot{x}(t) = (A - BK)x(t) \tag{43}$$

Then, Theorem 1 related to the closed-loop system (43) is given below.

Theorem 1. When standard assumptions are satisfied, the control obtained by minimizing the function (42) satisfies the system of (41), and the closed-loop system (43) is globally exponentially stable with

$$\lim_{t \to \infty} x(t)e^{\beta t} = 0. \tag{44}$$

Proof. Define $\bar{x}(t)$, $\bar{u}(t)$, \bar{A} , and \bar{B} by

$$\bar{x}(t)e^{\beta t}x(t), \ \bar{u}(t) = e^{\beta t}u(t), \ \text{and} \ \bar{A} = A + \beta I.$$
 (45)

A new continuous-time system can be formulated by

$$\dot{\bar{x}}(t) = \dot{x}(t)e^{\beta t} + \beta x e^{\beta t}$$

$$= (Ax(t) + Bu(t))e^{\beta t} + \beta x e^{\beta t}$$

$$= \bar{A}\bar{x}(t) + B\bar{u}(t).$$
(46)

Finally, the performance index of (42) can be rewritten by

$$\min_{\bar{u}} \int_0^\infty e^{2\beta\tau} (x(\tau)^T Q x(\tau) + u(\tau)^T R u(\tau)) d\tau$$

$$= \min_{\bar{u}} \int_0^\infty (\bar{x}(\tau)^T Q \bar{x}(\tau) + \bar{u}(\tau)^T R \bar{u}(\tau)) d\tau$$
(47)

Based on the above analysis, the problem of the optimal control defined by (41) and (42) can be converted to the problem of the traditional linear optimal control expressed by (46) and (47).

B. Review of Linear Quadratic Regulators

Problem 1 is an LQR problem, so the feedback gain is

$$K = R^{-1}B^TP (48)$$

where $P = P^T > 0$ can be found through solving the following algebraic Riccati equation (also known as ARE).

$$\bar{A}^T P + P \bar{A} + Q - P B R^{-1} B^T P = 0. \tag{49}$$

Algorithm 1 Value Iteration Algorithm

Initialization: Choose $P_0 = P_0^T > 0$, $j, q \leftarrow 0$, and $\tau > 0$. Define a ball B_q and a step size ϵ_j as follows

$$B_{q} \subseteq B_{q+1}, \quad q \in N, \quad \lim_{q \to \infty} B_{q} = \mathbb{P}_{+}^{n}$$

$$\epsilon_{j} > 0, \quad \sum_{j=0}^{+\infty} \epsilon_{j} = +\infty, \quad \sum_{j=0}^{+\infty} \epsilon_{j}^{2} < +\infty.$$
(50)

Value Evaluation: Solve for \bar{P}_{i+1} using

$$\bar{P}_{j+1} = P_j + \epsilon_j (\bar{A}^T P_j + P_j \bar{A} + Q - P_j B R^{-1} B^T P_j). \tag{51}$$

If $\bar{P}_{j+1} \notin B_q$, then $P_{j+1} \leftarrow P_0$, $q \leftarrow q+1$, else if $|\bar{P}_{j+1} - P_j|/\epsilon_j < \tau$ then $P_j = P^*$

Policy Improvement: Update the feedback gain matrix by

$$K^* = R^{-1}B^T P^*. (52)$$

The controller of the original system is

$$u(t) = -K^* \bar{x}(t) e^{-\beta t}. \tag{53}$$

Lemma 1. Considering $\{P_j\}$ and $\{K_j\}$ in Algorithm 1, it can approximate the solution to (49) with an assured convergence. As a result, $\lim_{t\to\infty} P_j = P_{j^*}$ and $\lim_{t\to\infty} K_j = K_{j^*}$.

Nonetheless, Algorithm 1 is based on the known value of the matrix and will not be implemented when the system matrix is uncertain or completely unknown. The following subsection shows how to use the value iteration method to design a controller with unknown system dynamics.

C. Adaptive, Optimal Control Design

To begin with, the following control policy is applied.

$$\bar{u}(t) = u_0(t) \tag{54}$$

where $u_0(t)$ can be chosen as any initializing control policy, and the system (46) can be rewritten as

$$\dot{\bar{x}}(t) = \bar{A}\bar{x}(t) + Bu_0(t). \tag{55}$$

Then, taking the time derivative of $\bar{x}(t)^T P_i \bar{x}(t)$ results in

$$\frac{d}{dt}\bar{x}(t)^T P_j \bar{x}(t) = \bar{x}(t)^T (\bar{A}^T P_j + P_j \bar{A}) \bar{x}(t)
+2u_0(t)^T B^T P_j \bar{x}(t)
= \bar{x}(t)^T Q_j \bar{x}(t)
+2u_0(t)^T R K_j \bar{x}(t)$$
(56)

where
$$Q_j=\bar{A}^TP_j+P_j\bar{A},\,RK_j=B^TP_j$$
 . During the time period of $[t,t+\delta t]$, (56) is rewritten as

$$\bar{x}(t+\delta t)^T P_j \bar{x}(t+\delta t) - \bar{x}(t)^T P_j \bar{x}(t)$$

$$= \int_t^{t+\delta t} \bar{x}_i(\tau)^T Q_j \bar{x}(\tau) d\tau$$

$$+2 \int_t^{t+\delta t} u_0(\tau)^T R K_j \bar{x}(\tau) d\tau. \tag{57}$$

Given $t_0 \leq t_1 \leq t_2 \cdots \leq t_s$, the following matrices are defined.

$$\begin{split} I_{\bar{x},\bar{x}} &= \left[\begin{array}{c} \int_{t_0}^{t_1} \text{vecv}(\bar{x}(\tau)) d\tau, \cdots, \int_{t_{s-1}}^{t_s} \text{vecv}(\bar{x}(\tau)) d\tau \end{array} \right]^T, \\ I_{\bar{x},\bar{u}} &= \left[\begin{array}{c} \int_{t_0}^{t_1} \bar{x} \otimes Ru_0 d\tau, \cdots, \int_{t_{s-1}}^{t_s} \bar{x} \otimes Ru_0 d\tau \end{array} \right]^T, \\ \Gamma_{\bar{x},\bar{x}} &= \left[\begin{array}{c} \text{vecv}(\bar{x}(\tau))|_{t_0}^{t_1}, \cdots, \text{vecv}(\bar{x}(\tau))|_{t_{s-1}}^{t_s} \end{array} \right]^T. \end{split}$$

Next, for any given P_0 , (57) represents the following matrix linear equation form.

$$\Psi \left[\begin{array}{c} \operatorname{vecs}(Q_j) \\ \operatorname{vec}(K_j) \end{array} \right] = \Gamma_{\bar{x},\bar{x}} \operatorname{vec}(P_j) \tag{58}$$

where $\Psi = \begin{bmatrix} I_{\bar{x},\bar{x}} & 2I_{\bar{x},\bar{u}} \end{bmatrix}$.

A sufficient condition that ensures the unique solution of the last equation is that the column Ψ of the matrix is full rank, as detailed in (59).

$$\operatorname{rank}(\Psi) = \frac{n(n+1)}{2} + mn. \tag{59}$$

Algorithm 2 Adaptive, Optimal Controller Design

Initialization: Choose $P_0 = P_0^T > 0$, initial control strategy $u_0(t)$ $j, q \leftarrow 0$, and $\tau > 0$

Data Collection: Collect online $I_{\bar{x},\bar{x}}$, $I_{\bar{x},\bar{x}}$, and $\Gamma_{\bar{x},\bar{x}}$. Solve for Q_j and K_j using:

$$\begin{bmatrix} \operatorname{vecs}(Q_j) \\ \operatorname{vec}(K_j) \end{bmatrix} = (\Psi^T \Psi)^{-1} \Psi \Gamma_{\bar{x},\bar{x}} \operatorname{vec}(P_j)$$
 (60)

then solve for \bar{P}_{i+1} using:

$$\bar{P}_{j+1} = P_j + \epsilon_j (Q_j + Q - K_j^T R K_j). \tag{61}$$

If $\bar{P}_{j+1} \notin B_q$, then $P_{j+1} \leftarrow P_0$, $q \leftarrow q+1$, else if $|\bar{P}_{j+1} - P_j|/\epsilon_j < \tau$ then $P_j = P_{j^*}$ and $K_j = K_{j^*}$. Apply $u(t) = -K_{j^*}\bar{x}(t)e^{-\beta t}$ as the controller.

The convergence of Algorithm 2 is guaranteed under the rank condition (59) (see [42]).

Theorem 2. If (59) is satisfied, then $\lim_{t\to\infty} P_j = P_{j^*}$, and $\lim_{t\to\infty} K_j = K_{j^*}$, where $\{P_j\}$ and $\{K_j\}$ are obtained from Algorithm 2.

Proof. If (59) is satisfied, (60) has the unique solution of (Q_j, K_j) . According to (61), P_{j+1} and \bar{P}_{j+1} can uniquely be determined and are equivalent to the ones in Algorithm 1. Otherwise, there exists a different pair (Q'_j, K'_j) satisfying (60). Lemma 1 proves the convergences of $\{P_j\}$ and $\{K_j\}$. The proof of Theorem 2 is now completed.

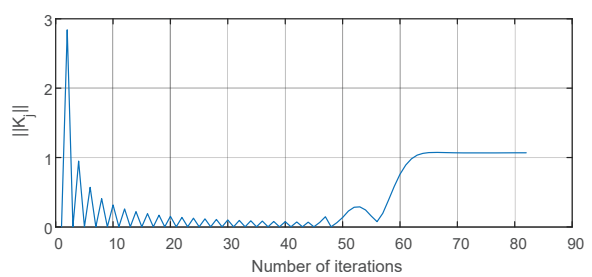


Fig. 4. Convergence of K_j to their optimal values K^* during the learning process.

D. Stability Analysis

In order to study the influence of the control strategy in this paper on the transient stability of the system, this paper uses Lyapunov's second method to analyze the stability of the ADP-based VSG control strategy.

The system (46) in the closed-loop system with the controller $\bar{u}(t) = -K_i \bar{x}(t)$ is

$$\bar{x} = (\bar{A} - BK_i)\bar{x}(t). \tag{62}$$

Define a Lyapunov function as

$$V(x) = \bar{x}(t)^T P \bar{x}(t). \tag{63}$$

Then, taking the time derivative of V(x) results in

$$\frac{d}{dt}V(x) = \frac{d}{dt}\bar{x}^T P \bar{x} + \bar{x}^T P \frac{d}{dt}\bar{x}$$

$$= -\bar{x}^T (Q + PBR^{-1}B^T P)\bar{x}.$$
(64)

Since Q is a positive semi-definite, symmetric matrix and the elements q_1 and q_2 are positive, P and R are both positive definite symmetric matrices. Then, one can obtain

$$\frac{d}{dt}V(x) \le 0. (65)$$

If and only if $\bar{x}(t)=0$, the equal sign in (64) is true. According to the Lyapunov stability theorem, the equilibrium state $\bar{x}(t)=0$ is uniformly asymptotically stable. This matter implies that $\lim_{t\to\infty}\bar{x}(t)=0$, and the convergence rate of x(t) is no slower than $e^{-\beta t}$. The proof is thus completed.

VII. SIMULATION RESULTS

In order to verify the effectiveness of the proposed algorithm and avoid the interference caused by the control parameters, comparative simulations under multiple sets of control parameters are carried out. The system parameters are: $L_f=6$ mH, $r_f=0.056~\Omega,~L_g=4.8$ mH, $r_g=0.1~\Omega,~C=50~\mu\text{F},~P_{\text{ref}}=8$ kW, $Q_{\text{ref}}=0$ kvar, $\omega_g=100\pi$ rad/s, $E_g=220$ V (line-to-neutral rms value), $K_p=0.0001,~K_i=0.03$, and $Q=\begin{bmatrix}1&0\\0&1\end{bmatrix},~R=40,~\beta=4.$

According to the optimal damping ratio method, the VSG parameters can be set to $J_o = 5$ and $D_o = 42$. The convergence of $\{K_j\}$ to their optimal values is illustrated in Fig. 4. The results show that after 83 iterations, the feedback control gain obtained by ADP is the approximate optimal feedback gain.

The control gain K updated after 83 iterations is

$$K_{83} = \begin{bmatrix} 1.1198 & 0.1805 \end{bmatrix}.$$
 (66)

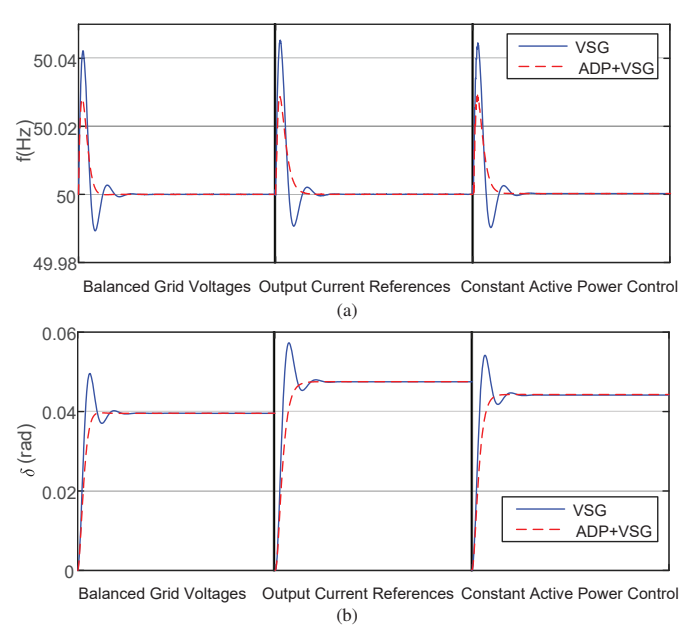


Fig. 5. Comparison of output between traditional VSG and ADP+VSG: (a) output frequency, (b) output power angle.

A. Working Condition #1: Balanced and Unbalanced Grids

For Working Condition #1, the system works under balanced and unbalanced grid conditions. Comparing the output between traditional VSG and ADP+VSG under $J_o=5$, $D_o=42$ in Fig. 5. The figure on the left shows the control under the balanced grid, the middle figure shows the reference current control under the unbalanced grid, and the figure on the right shows the constant active power control under the unbalanced grid. As shown in Fig. 5, the output power angle and output frequency of ADP+VSG are lower than the traditional VSG overshoot, and the response is faster.

Output of other physical quantities under various conditions is shown in Fig. 6. As depicted in Fig. 5, the output power reference tracking can be guaranteed under the grid voltage balance, reference current control can ensure current balance under unbalanced grid voltage, and constant active power control under unbalanced grid voltage can suppress output active power oscillation (within ± 200 W).

Fig. 7 shows the control parameter perturbation $\pm 20\%$, $\pm 40\%$, $\pm 60\%$, and $\pm 80\%$, i.e., $J_m = nJ_o$ and $D_m = nD_o$ for $n \in \{0.2, 0.4, 0.6, 0.8, 1, 1.2, 1.4, 1.6, 1.8\}$. The results show that when the control parameters are perturbed, the ADP-optimized VSG still has a smaller overshoot.

B. Working Condition #2: Voltage Drop/Sag

Initially, the VSG is connected to a grid with nominal voltages without any voltage drop/sag. Then, at $t=5\,\mathrm{s}$, the voltage is dropped by 10%, 15%, 20%, and 25% for 0.75 s. Fig. 8 shows the comparison between the output of the traditional VSG and ADP+VSG under $J_o=5$, $D_o=42$. It is evident that as the grid voltage drops more, the traditional ADP oscillates more during voltage drops. Also, the greater the oscillation after returning to the normal voltage, the longer the recovery time. ADP+VSG can, however, effectively suppress the oscillation, especially during recovery, with a better performance.

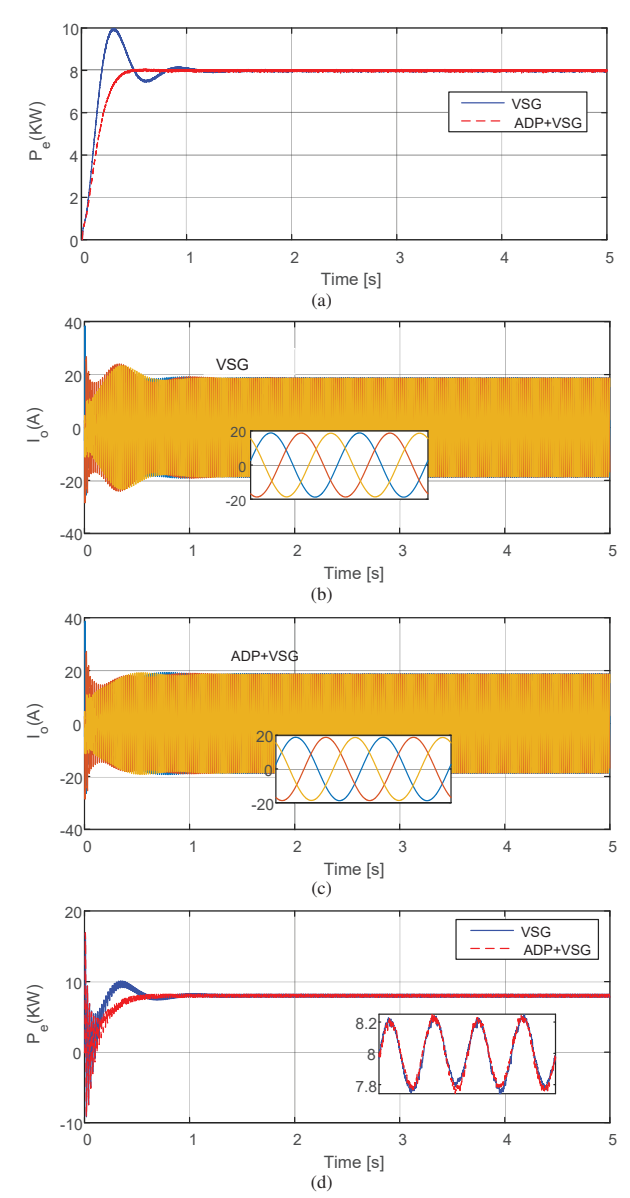


Fig. 6. Other output variables under various conditions: (a) active power under grid voltage balance, (b) current under traditional VSG reference current control, (c) current under ADP+VSG reference current control, and (d) active power under constant active power control.

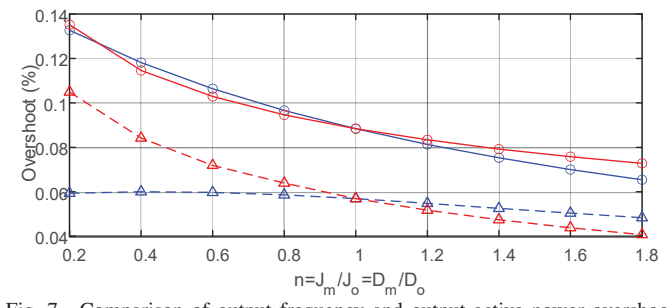


Fig. 7. Comparison of output frequency and output active power overshoot under parameter perturbation: output frequency overshoot—the blue line represents the damping change, and the red line represents the inertia change; "o" and " Δ " indicate traditional VSG and ADP+VSG, respectively.

C. Working Condition #3: Weak-Grid Conditions

In this subsection, the weak-grid conditions with different short-circuit ratios [also known as SCRs or short-circuit ca-

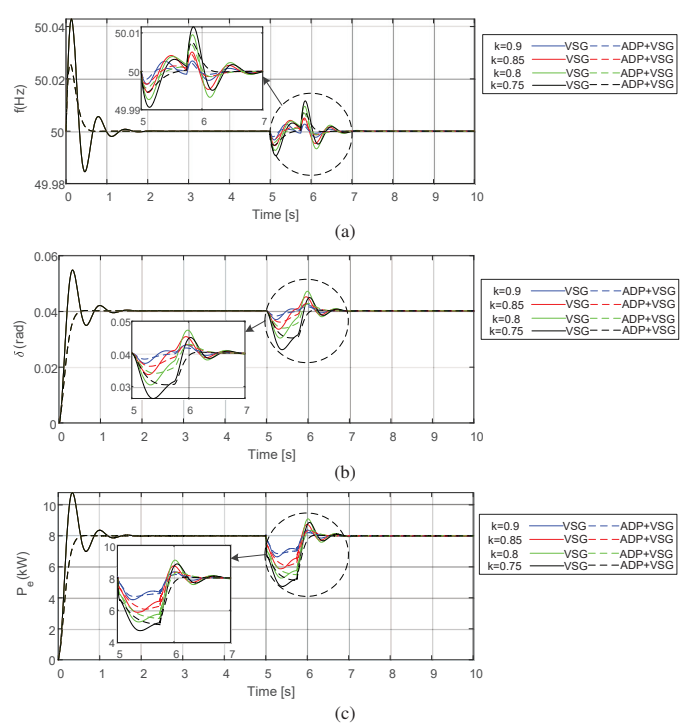


Fig. 8. Comparison between the output of the traditional VSG and ADP+VSG under 10%–25% voltage drop cases: (a) VSG-controlled output frequency, (b) VSG-controlled output power angle, and (c) output active power.

pacity ratios (SCCRs) [26]] are set. The results are shown in Fig. 9. It illustrates that as SCR decreases, the traditional VSG oscillates more and more—even it exceeds the converter limit of 10 kVA. Although there are some oscillations in ADP+VSG, the amplitude is much lower than that of the traditional VSG; they are normal in weak-grid conditions without advanced controls—especially for SCR=1 [25], [26].

VIII. EXPERIMENTAL RESULTS

The test setup depicted in Fig. 10 has been employed to conduct experimental examinations. It is built by SEMIKRON intelligent power modules using insulated gate bipolar transistors (IGBTs) (based on "SKM 50 GB 123 D" modules). Besides, SEMIKRON "SKHI 21A (R)" gate drives and protection circuitry are utilized in order to make the converter functional. Current/voltage transducers have been hooked to digital inputs to measure current/voltage signals. dSPACE "MicroLabBox (MLBX)" using a real-time processor and field-programmable gate arrays (commonly known as FPGAs) and benefiting from PWM signals (generated by digital inputs/outputs) connects the VSC under test to the printed circuit boards of the measurement and drive circuits. The dSPACE MLBX interface board is equipped with analog-to-digital channels to interface the measured signals to the controller. Furthermore, in order to make the point of common coupling (also known as PCC), 4quadrant voltage amplifiers from Spitzenberger & Spies (APS type) are deployed in the test setup.

For the experimental results, the simulation procedure detailed in Section VII-A has been replicated as a representative case to reveal the effectiveness of the proposed methodology. The parameters of the used test rig have been matched to

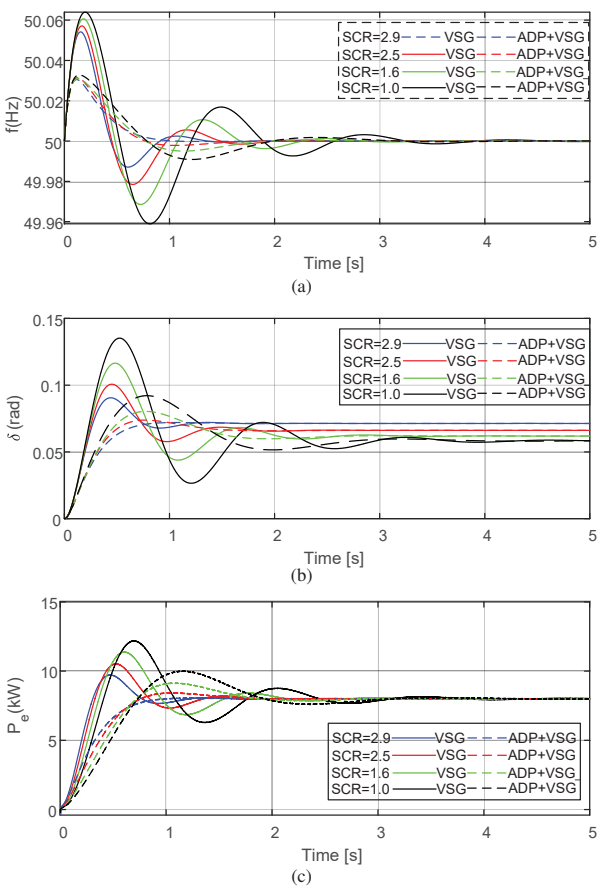
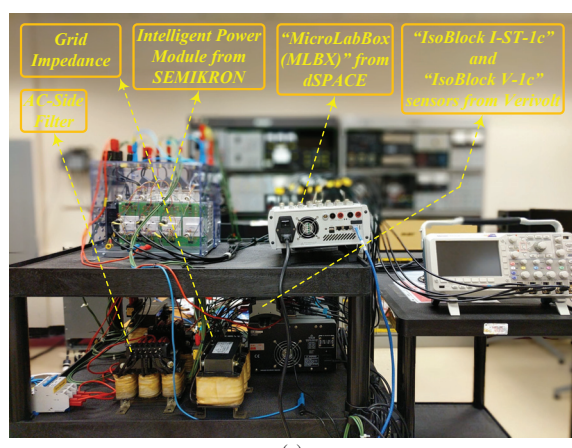


Fig. 9. Comparison of output between traditional VSG and ADP+VSG under weak-grid conditions: (a) output frequency, (b) output power angle, and (c) output active power.

those employed in simulations as much as possible. Therefore, a comparison between simulation and experiment results is feasible. Fig. 11 shows the experimental outcomes of the proposed method. Simulations and experiments match well with each other. The demonstrated agreement in simulations and experiments, which are consistent all together, reveals the effectiveness of the proposed ADP control for VSGs. In Fig. 11, traces in blue [Channel (Ch.) #1], cyan (Ch. #2), magenta (Ch. #3), and lawn green (Ch. #4) have been assigned to the frequency signal (for "ADP+VSG"), the frequency signal (for "VSG"), the power signal (for "ADP+VSG"), and the power signal (for "VSG"), respectively. It is noteworthy that because the percentage of frequency fluctuations is minuscule compared to the dc component of the frequency signal, it is required to capture the ac component of the frequency signal (equivalent to the dc input coupling setting in oscilloscopes) to be able to show frequency transients. The caption of Fig. 11 details information on different channels.

IX. CONCLUSION

In this paper, an approach based on adaptive dynamic programming has been developed in order to synthesize an adaptive, optimal controller for VSGs. It can reduce the oscillation of VSG while maintaining the system stability for the closed-loop inverter. An optimal control strategy for VSG has been proposed in order to have power/frequency control. Also, the frequency and power oscillation problems have been



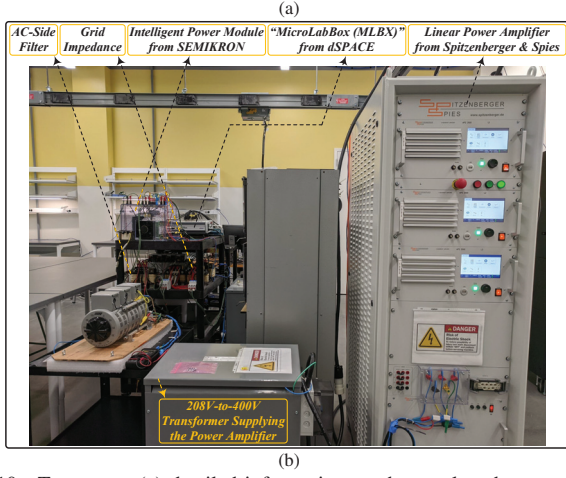


Fig. 10. Test setup: (a) detailed information on the employed converter and (b) arrangement of the deployed power components.

successfully solved by having a single VSG connected to the grid and optimizing parameters.

Comparative simulations and experimental results have revealed that without knowing the control parameters in the VSG, the developed controller can reduce the system's oscillation and improve the overall control performance. When the original system parameter configuration is ideal, ADP control will further improve system performance. In the case of unbalanced grid voltages, voltage drops/sags, and weak-grid conditions, the use of ADP control has also enhanced results.

ACKNOWLEDGEMENT

The authors would like to say a big thank you to Professor Zhong-Ping Jiang in the Control and Network (CAN) Lab at New York University for his pieces of constructive feedback, advice, and insightful comments.

REFERENCES

- [1] S. Yazdani, M. Davari, M. Ferdowsi, and P. Shamsi, "Internal model power synchronization control of a PV-based voltage-source converter in weak-grid and islanded conditions," *IEEE Trans. Sustain. Energy*, vol. 12, no. 2, pp. 1360–1371, Apr. 2021.
- [2] R. V. Ferreira, S. M. Silva, H. M. A. Antunes, and G. Venkataramanan, "Dynamic analysis of grid-connected droop-controlled converters and synchronverters," *J. Control Autom. Electr. Syst.*, vol. 30 (2019), pp. 741–753, Jun. 2019.

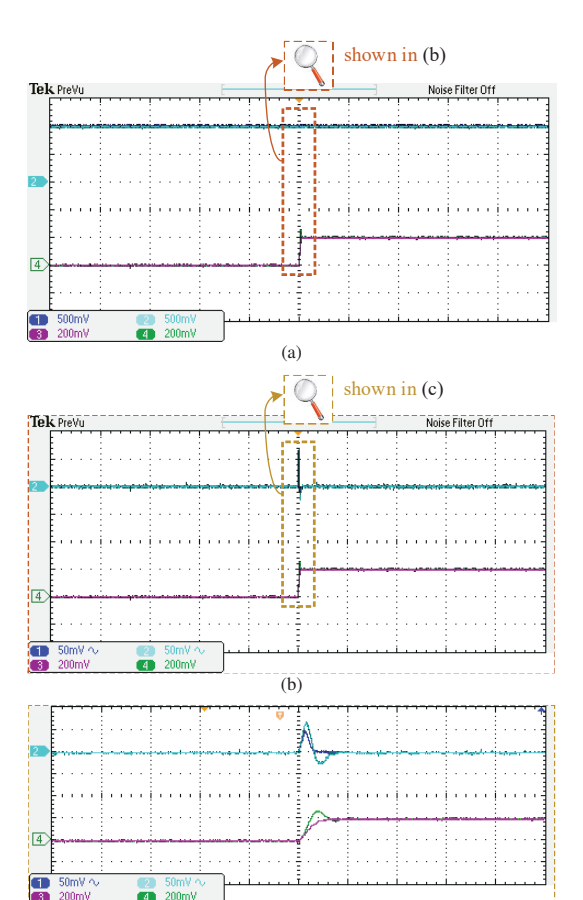


Fig. 11. Experimental results associated with an increase in active power while showing grid frequency: (a) 25 Hz/div for frequency [dc component of Channels (Chs.) #1 and #2, or equivalently dc input coupling setting], 8.00 kW/div for power (dc component of Chs. #3 and #4), and 10 s/div for horizontal axis; (b) the ac components of the frequency signals depicted in Fig. 11a with 0.025 Hz/div for frequency (ac component of Chs. 1 and 2, or equivalently ac input coupling setting), 8.00 kW/div for power (dc component of Chs. #3 and #4), and 10 s/div for horizontal axis; and (c) the enlarged view of the signals depicted in Fig. 11b with 0.025 Hz/div for frequency (ac component of Chs. 1 and 2), 8.00 kW/div for power (dc component of Chs. #3 and #4), and 800 ms/div for horizontal axis.

- [3] N. D. Tuyen, G. Fujita, T. Funabashi, and M. Nomura, "Analysis of transient-to-island mode of power electronic interface with conventional *dq*-current controller and proposed droop-based controller," *Electr. Eng.*, vol. 99 (2017), pp. 47–57, Jun. 2016.
- [4] B. K. Unnikrishnan, M. S. Johnson, and E. P. Cheriyan, "Small signal stability improvement of a microgrid by the optimised dynamic droop control method," *IET Renew. Power Gener.*, vol. 14, no. 5, pp. 822–833, Aug. 2019.
- [5] M. A. Ghalib, E. G. Shehat, J. Thomas, and R. M. Mostafa, "Adaptive droop control for high-performance operation in low-voltage DC microgrids," *Electr. Eng.*, vol. 101 (2019), pp. 1311–1322, Nov. 2019.
- [6] F. Katiraei, R. Iravani, N. Hatziargyriou, and A. Dimeas, "Microgrids management," *IEEE Power and Energy Magazine*, vol. 6, no. 3, pp. 54–65, May/Jun. 2008.
- [7] R. Shi, X. Zhang, C. Hu, H. Xu, J. Gu, and W. Cao, "Self-tuning virtual synchronous generator control for improving frequency stability in autonomous photovoltaic-diesel microgrids," *J. Mod. Power Syst.* Clean Energy, vol. 6 (2018), pp. 482–494, May 2018.
- [8] W. Cao, K. Liu, S. Xu, H. Kang, and J. Zhao, "Stabilization control strategy for shore power system with surge loads based on virtual synchronous generator," J. Electr. Eng. Technol., vol. 14, no. 3, pp. 1045–1054, May 2019.
- [9] K. Dhingra and M. Singh, "Frequency support in a micro-grid using virtual synchronous generator based charging station," *IET Renew. Power Gener.*, vol. 12, no. 9, pp. 1034–1044, Jun. 2018.
- [10] Y. Daili and A. Harrag, "New model of multi-parallel distributed

- generator units based on virtual synchronous generator control strategy," *Energ. Ecol. Environ.*, vol. 4 (2019), pp. 222–232, Aug. 2019.
- [11] K. Sundaramoorthy, V. Thomas, T. O'Donnell, and S. Ashok, "Virtual synchronous machine-controlled grid-connected power electronic converter as a ROCOF control device for power system application," *Electr. Eng.*, vol. 101, no. 3, pp. 983–993, Sep. 2019.
- [12] F. Yao, J. Zhao, X. Li, L. Mao, and K. Qu, "RBF neural network based virtual synchronous generator control with improved frequency stability," *IEEE Trans. Ind. Inform.*, vol. 17, no. 6, pp. 4014–4024, Jun. 2020.
- [13] V. L. Srinivas, B. Singh, and S. Mishra, "Seamless mode transition technique for virtual synchronous generators and method thereof," *IEEE Trans. Ind. Inform.*, vol. 16, no. 8, pp. 5254–5266, Aug. 2020.
- [14] Q. C. Zhong, G. C. Konstantopoulos, B. Ren, and M. Krstic, "Improved synchronverters with bounded frequency and voltage for smart grid integration," *IEEE Trans. Smart Grid*, vol. 9, no. 2, pp. 786–786, Mar. 2018
- [15] Z. Shuai, Y. Hu, Y. Peng, C. Tu, and Z. J. Shen, "Dynamic stability analysis of synchronverter-dominated microgrid based on bifurcation theory," *IEEE Trans. Ind. Electron.*, vol. 64, no. 9, pp. 7467–7477, Sep. 2017.
- [16] F. Wang, L. Zhang, X. Feng, and H. Guo, "An adaptive control strategy for virtual synchronous generator," *IEEE Trans. Ind. Appl.*, vol. 54, no. 5, pp. 5124–5133, Sep./Oct. 2018.
- [17] T. Shintai, Y. Miura, and T. Ise, "Oscillation damping of a distributed generator using a virtual synchronous generator," *IEEE Trans. Power Deliv.*, vol. 29, no. 2, pp. 668–676, Apr. 2014.
- [18] D. Li, Q. Zhu, S. Lin, and X. Y. Bian, "A self-adaptive inertia and damping combination control of VSG to support frequency stability," *IEEE Trans. Energy Convers.*, vol. 32, no. 1, pp. 397–398, Mar. 2017.
- [19] H. Geng, C. Liu, and G. Yang, "LVRT capability of DFIG-based WECS under asymmetrical grid fault condition," *IEEE Trans. Ind. Electron.*, vol. 60, no. 6, pp. 2495–2509, Jun. 2013.
- [20] M. R. Alam and K. M. Muttaqi, "Characterizing voltage sags and swells using three-phase voltage ellipse parameters," *IEEE Trans. Ind. Appl.*, vol. 51, no. 4, pp. 2780–2790, Jul./Aug. 2015.
- [21] J. Alipoor, Y. Miura, and T. Ise, "Power system stabilization using virtual synchronous generator with alternating moment of inertia," *IEEE J. Emerg. Sel. Topics Power Electron.*, vol. 3, no. 2, pp. 451–458, Jun. 2015
- [22] Z. Shuai, W. Huang, C. Shen, J. Ge, and Z. J, Shen, "Characteristics and restraining method of fast transient inrush fault currents in synchronverters," *IEEE Trans. Ind. Electron.*, vol. 64, no. 9, pp. 7487–7497, Sep. 2017.
- [23] J. Liu, Y. Miura, and T. Ise, "Comparison of dynamic characteristics between virtual synchronous generator and droop control in inverterbased distributed generators," *IEEE Trans. Power Electron.*, vol. 31, no. 5, pp. 3600–3611, May 2016.
- [24] A. D. Paquette and D. M. Divan, "Virtual impedance current limiting for inverters in microgrids with synchronous generators," *IEEE Trans. Ind. Appl.*, vol. 51, no. 2, pp. 1630–1638, Mar./Apr. 2015.
- [25] M. Davari, M. P. Aghababa, F. Blaabjerg, and M. Saif, "A modular adaptive robust nonlinear control for resilient integration of VSIs into emerging modernized microgrids," *IEEE J. Emerg. Sel. Topics Power Electron.*, vol. 9, no. 3, pp. 2907–2925, Jun. 2021.
- [26] M. Davari and Y. A.R.-I Mohamed, "Robust vector control of a very weak-grid-connected voltage-source converter considering the phaselocked loop dynamics," *IEEE Trans. Power Electron.*, vol. 32, no. 1, pp. 977–994, Feb. 2017.
- [27] X. Wang, Y. W. Li, and F. Blaabjerg, "Virtual-impedance-based control for voltage-source and current-source converters," *IEEE Trans. Power Electron.*, vol. 30, no. 12, pp. 7019–7037, Dec. 2015.
- [28] U. Markovic, Z. Chu, P. Aristidou, and G. Hug, "LQR-based adaptive virtual synchronous machine for power systems with high inverter penetration," *IEEE Trans. Sustain. Energy*, vol. 10, no. 3, pp. 1501– 1512, Jul. 2019.
- [29] R. S. Sutton and A. G. Barto, "Reinforcement learning: An introduction," Cambridge, MA, USA: MIT Press, 2018.
- [30] S. Wu, W. Hu, Z. Lu, Y. Gu, and B. Tian, "Power system flow adjustment and sample generation based on deep reinforcement learning," *J. Mod. Power Syst. Clean Energy*, vol. 8, no. 6, pp. 1115–1127, Nov. 2020.
- [31] O. Nassef, L. Sequeira, E. Salam, and T. Mahmoodi, "Building a lane merge coordination for connected vehicles using deep reinforcement learning," *IEEE Internet Things J.*, vol. 8, no. 4, pp. 2540–2557, Feb. 15, 2020.
- [32] Y. Jiang, J. Fan, T. Chai, J. Li, and F. L. Lewis, "Data-driven flotation industrial process operational optimal control based on reinforcement

- learning," *IEEE Trans. Ind. Inform.*, vol. 14, no. 5, pp. 1974–1989, May 2018.
- [33] Y. Jiang and Z. -P. Jiang, "Global adaptive dynamic programming for continuous-time nonlinear systems," *IEEE Trans. Autom. Control*, vol. 60, no. 11, pp. 2917–2929, Nov. 2015.
- [34] T. Sun and X. M. Sun, "An adaptive dynamic programming scheme for nonlinear optimal control with unknown dynamics and its application to turbofan engines," *IEEE Trans. Ind. Inform.*, vol. 17, no. 1, pp. 367–376, Jan. 2021.
- [35] A. Saberi, A. A. Stoorvogel, P. Sannuti, and G. Shi, "On optimal output regulation for linear systems," *Int. J. Control*, vol. 76, no. 4, pp. 319– 333, Nov. 2010.
- [36] W. Gao and Z.-P. Jiang, "Adaptive dynamic programming and adaptive optimal output regulation of linear systems," *IEEE Trans. Autom. Control*, vol. 61, no. 12, pp. 4164–4169, Dec. 2016.
- [37] T. Nguyen and Z. Gajic, "Solving the matrix differential riccati equation: A Lyapunov equation approach," *IEEE Trans. Autom. Control*, vol. 55, no. 1, pp. 191–194, Jan. 2010.
- [38] S. Sen and V. Kumar, "Decentralized output-feedback-based robust LQR V-f controller for PV-battery microgrid including generation uncertainties," IEEE Syst. J., vol. 14, no. 3, pp. 4418–4429, Sep. 2020.
- [39] X. K. Liu, H. Jiang, Y. W. Feng, and H. He, "A distributed iterative learning framework for DC microgrids: Current sharing and voltage regulation," *IEEE Trans. Emerg. Topics Comput. Intell.*, vol. 4, no. 2, pp. 119–129, Apr. 2020.
- [40] M. Davari, W. Gao, Z.-P. Jiang, and F. L. Lewis, "An optimal primary frequency control based on adaptive dynamic programming for islanded modernized microgrids," *IEEE Trans. Autom. Sci. Eng.*, vol. 18, no. 3, pp. 1109–1121, Jul. 2021.
- [41] S. Xue, B. Luo, D. Liu, and Y. Li, "Adaptive dynamic programming based event-triggered control for unknown continuous-time nonlinear systems with input constraints," *Neurocomputing*, vol. 396 (2020), pp. 191–200, Jul. 2020.
- [42] T. Bian and Z.-P. Jiang, "Value iteration and adaptive dynamic programming for data-driven adaptive optimal control design," *Automatica*, vol. 71 (2016), pp. 348–360, Sep. 2016.
- [43] B. Luo, Y. Yang, and D. Liu, "Policy iteration Q-Learning for data-based two-player zero-sum game of linear discrete-time systems," *IEEE Trans. Cybern.*, vol. 51, no. 7, pp. 3630–3640, Jul. 2021.
- [44] S. Wang, X. Jin, S. Mao, A. V. Vasilakos, and Y. Tang, "Model-free event-triggered optimal consensus control of multiple euler-lagrange systems via reinforcement learning," *IEEE Trans. Netw. Sci. Eng.*, vol. 8, no. 1, pp. 246–258, Jan./Mar. 2021.
- [45] K. Zhang and S. L. Ge, "Adaptive optimal control with guaranteed convergence rate for continuous-time linear systems with completely unknown dynamics," *IEEE Access*, vol. 7, pp. 11 526–11 532, Feb. 2019.
- [46] S. M. Shahruz, G. Langari, and M. Tomizuka, "Optimal damping ratio for linear second-order systems," *Journal of Optimization Theory and Applications*, vol. 73 (1992), pp. 563–576, 1992.
- [47] S. Y. Altahir, X. Yan, and A. S. Gadaalla, "New control scheme for virtual synchronous generators of different capacities," in *Proc. of the IEEE Int. Conf. on Energy Internet (ICEI)*, 2017, pp. 131–135.
- [48] M. Davari, M. P. Aghababa, F. Blaabjerg, and M. Saif, "An innovative, adaptive faulty signal rectifier along with a switching controller for reliable Primary control of GC-VSIs in CPS-based modernized microgrids," *IEEE Trans. Power Electron.*, vol. 36, no. 7, pp. 8370–8387, Jul. 2021.



Zhongyang Wang was born in Chuzhou, China. He received the B.Sc. degree in Automation from the East China University of Technology in 2017 and the M.Sc. degree in Control Science and Engineering from the Nanchang University in 2020. He is currently an Assistant Lecturer with the School of Applied Science and Engineering, Fuzhou Institute of Technology, China. His research interests include adaptive dynamic programming, optimal control of linear systems, and control of power systems.



Yunjun Yu (M'12) was born in Shangrao, China. He received the B.Sc. degree in Automation and the M.Sc. degree in Control Theory and Control Engineering from the Nanchang University in 2000 and 2007, respectively, and the Ph.D. degree from the Chinese Academy of Sciences in 2013. He is currently an Associate Professor with the Department of Automation, Information Engineering School, Nanchang University, China. His research interests include fault diagnosis, active disturbance rejection control (ADRC), data-driven optimal control and its

applications in microgrids, and low-carbon electricity technology.



Weinan Gao (M'18) received the B.Sc. degree in Automation from Northeastern University, Shenyang, China, in 2011, the M.Sc. degree in Control Theory and Control Engineering from Northeastern University, Shenyang, China, in 2013, and the Ph.D. degree in Electrical Engineering from New York University, Brooklyn, NY, in 2017. He is an Assistant Professor of Mechanical and Civil Engineering at Florida Institute of Technology, Melbourne, FL, since 2020. Previously, he was an Assistant Professor of Electrical and Computer Engi-

neering at Georgia Southern University, Statesboro, GA, in 2017–2020, and a Visiting Professor of Mitsubishi Electric Research Laboratory, Cambridge, MA, in 2018. His research interests include reinforcement learning, adaptive dynamic programming, optimal control, cooperative adaptive cruise control, intelligent transportation systems, sampled-data control systems, and output regulation theory. He is the recipient of the best paper award in IEEE International Conference on Real-time Computing and Robotics in 2018 and the David Goodman Research Award at New York University in 2019.

Dr. Gao is an Associate Editor or a Guest Editor of IEEE/CAA Journal of Automatica Sinica, Neurocomputing, IEEE Transactions on Neural Network and Learning Systems, and Complex & Intelligent Systems, a member of the Editorial Board of Neural Computing and Applications and Control Engineering Practice, a Program Committee Member in 2022 American Control Conference, and a Technical Committee Member in IEEE Control Systems Society on Nonlinear Systems and Control and in IFAC TC 1.2 Adaptive and Learning Systems, and IC 2.3 Non-Linear Control Systems.



Masoud Davari (GS'08–M'16–SM'19) was born in Isfahan, Iran, on Sep. 14, 1985. He received the B.Sc. degree (with distinction) in electrical engineering- power from the Isfahan University of Technology, Isfahan, Iran, in September 2007, the M.Sc. degree (with distinction) in electrical engineering-power from the Amirkabir University of Technology (Tehran Polytechnic), Tehran, Iran, in January 2010, and the Ph.D. degree in electrical engineering-energy systems from the University of Alberta, Edmonton, AB, Canada, in January 2016.

He was with Iran's Grid Secure Operation Research Center and Iran's Electric Power Research Institute (EPRI) in Tehran, Iran, from January 2010 to December 2011. From April 2015 to June 2017, he was working with Quanta-Technology Company, Markham, ON, Canada, in the field of the dynamic interaction of renewable energy systems with smart grids as well as control, protection, and automation of microgrids as a Senior R & D Specialist and Senior Consultant. In July 2017, he joined the Department of Electrical and Computer Engineering as a tenure-track Assistant Professor in the Allen E. Paulson College of Engineering and Computing at Georgia Southern University, Statesboro, GA, USA—where he was recommended and approved for being granted "early" promotion to Associate Professor and award of "early" tenure on December 03, 2021. He is the Founder and Director of the Laboratory for Advanced Power and Energy Systems (LAPES) in the stateof-the-art Center for Engineering and Research (CEaR) established in 2021 at Georgia Southern University. He has developed and implemented several experimental test rigs for research universities and the power and energy industry. He has also authored several IEEE Transactions and Journals. His research interests include the dynamics, controls, and protections of different power electronic converters, which are utilized in the hybrid ac/dc smart grids, and hardware-in-the-loop (HIL) simulation-based testing of modernized power

Dr. Davari has been serving as an active member and a chapter lead in the IEEE Power & Energy Society Task Force on "Innovative Teaching Methods for Modern Power and Energy Systems" since July 2020; he is also an active member and a chapter lead (for Chapter 3) in the IEEE Working Group P2004—a newly established IEEE working group entitled "Hardwarein-the-Loop (HIL) Simulation Based Testing of Electric Power Apparatus and Controls" for IEEE Standards Association—since June 2017. He is an invited member of the Golden Key International Honour Society. He served as the Chair of the Literature Review Subgroup of DC@Home Standards for the IEEE Standards Association from April 2014 to October 2015. He is an invited reviewer of several of the IEEE TRANSACTIONS and JOURNALS, IET journals, Energies Journal, and various IEEE conferences, as well as the invited speaker at different universities and in diverse societies and the Best Reviewer of the IEEE TRANSACTIONS ON POWER SYSTEMS in 2018 and 2020. He was the recipient of the 2019-2020 Allen E. Paulson College of Engineering and Computing (CEC) Faculty Award for Outstanding Scholarly Activity in the Allen E. Paulson CEC at Georgia Southern University and the winner of the 2020-2021 Discovery & Innovation Award from the University Awards of Excellence at Georgia Southern University.



Chao Deng (M'20) received the Ph.D. degree in control engineering from Northeastern University, China, in 2018. From May 2018 to May 2021, he was a Research Fellow at the School of Electrical and Electronic Engineering at Nanyang Technological University, Singapore. Currently, he is a faculty at the Institute of Advanced Technology, Nanjing University of Posts and Telecommunications, China. His research interests include distributed secondary control of microgrids and cyber-physical systems.